UNIVERSITY OF LATVIA

Summary of Doctoral Thesis

Līga Jasulaņeca

ON-CHIP NANOELECTROMECHANICAL SWITCHES FOR OPERATION AT ROOM AND CRYOGENIC TEMPERATURES

Riga 2024

UNIVERSITY
OF LATVIA

FACULTY OF PHYSICS, MATHEMATICS AND OPTOMETRY

Līga Jasulaņeca

ON-CHIP NANOELECTROMECHANICAL SWITCHES FOR OPERATION AT ROOM AND CRYOGENIC TEMPERATURES

SUMMARY OF THE DOCTORAL THESIS

Submitted for the degree of Doctor of Science (Ph.D.) in Natural Sciences

Field of Physics and Astronomy

Subfield of Materials Physics

Riga 2024

The doctoral thesis was carried out at the Institute of Chemical Physics, University of Latvia, from year 2020 to 2024.

The creation of this thesis was supported by FLPP lzp-2019/1-0349, ESF 8.2.2.0/20/I/006 projects and MikroTik grant, administered by UL Foundation.

Form of the thesis: dissertation in Physics and Astronomy, subfield of Materials Physics.

Supervisor: Prof. Dr. chem. **Donats Erts,** University of Latvia, Institute of Chemical Physics, Latvia.

Reviewers:

1) Prof. Dr. phys. **Anatolijs Sarakovskis, U**niversity of Latvia, Latvia;
2) Prof. Dr. sc. ing. **Andris Sutka,** Riga Technical University, Latvia;
3) Asoc. Prof. Dr. phys. **Rynno Lohmus,** University of Tartu, Estonia.

The thesis will be defended at the public session of the Doctoral Committee of Physics and astronomy, University of Latvia, on 17th September 2024 at 14.00, Institute of Solid State Physics, University of Latvia, Kengaraga Street 8, Riga.

The thesis is available at the Library of the University of Latvia, Raina blvd. 19.

Chairman of the Doctoral Committee: Prof. Dr. habil. phys. **Linards Skuja.**

Secretary of the Doctoral Committee: **Sintija Silina.**

ISBN 978-9934-36-260-6
ISBN 978-9934-36-261-3 (PDF)

ABSTRACT

The demand for low-power portable devices has led to a search for alternatives to the fundamental component of computing and logic – the electronic transistor. Nanoelectromechanical (NEM) switches are one such alternative device whose leakage current in the off state is negligible because the current-carrying components are physically separated. The exploration of these switches at low temperatures is motivated by their potential applications in space and quantum technologies.

Researchers are considering bottom-up synthesized 1D nanostructures as future electronic components due to their high quality and material diversity. However, these nanostructures exhibit significant variation in morphology and electromechanical properties, making their application in integrated NEM switches challenging. Another challenge is their integration with the existing planar technology.

To overcome this, this thesis investigates copper oxide (CuO), bismuth selenide (Bi_2Se_3), and germanium (Ge) semiconductor 1D nanostructures as active elements in NEM switches. This study aims to develop switch technology and expand its applications using the unique properties of semiconductor nanostructures grown by the bottom-up method. The work involves synthesizing nanostructures, characterizing their morphology, electrical and mechanical properties, transferring and aligning them onto substrates, and creating and characterizing NEM switches at room and cryogenic temperatures.

NEM switch operation is studied *in situ* in a scanning electron microscope and in integrated devices. The fabricated integrated NEM switches demonstrate repeated switching, implementing both logic and memory functions. The switch operation is achieved at room temperature and down to 2 K, with a minimum switch-ON voltage of 4.5 V and a maximum ON/OFF state current ratio of 10^3. A novel type of NEM switch is demonstrated whose operation can be controlled by measuring the current that flows through a Bi_2Se_3 nanobelt during deformation.

The results presented in this study open possibilities for developing faster and more robust memory and mechanical computing devices, as well as more sensitive sensors for a wide range of operational temperatures.

The results are published in 11 scientific papers.

Keywords: nanoelectromechanical switches, nanowires, nanobelts, cryogenic temperatures, Bi_2Se_3, CuO, Ge

TABLE OF CONTENTS

NOMENCLATURE

Abbreviations

1D NS	one-dimensional nanostructure/-s
2T	two-terminal
3T	three-terminal
AC	alternating current
AFM	atomic force microscope
Bi_2Se_3	bismuth selenide
CMOS	complementary metal oxide semiconductor
CuO	copper oxide
D	drain electrode
DC	direct current
FET	field effect transistor
G	gate electrode
Ge	germanium
MEM	microelectromechanical
NEM	nanoelectromechanical
NS	nanostructure/-s
NW	nanowire/-s
S	source electrode
SdH	Shubnikov-de Haas (oscillations/frequencies)
SEM	scanning electron microscope
SS	sub-threshold slope
TI	topological insulator
WAL	weak anti-localization

Selected symbols and units

A	area [m^2]
B	magnetic field [T]
d	diameter [m]
E	Young's modulus [GPa]
f	frequency [Hz]
L	length [m]
R	resistance [Ω]
t	thickness [m]
w	width [m]
z	heigh/depth of a G electrode [m]

1. INTRODUCTION

1.1. General introduction and motivation

Nanoelectromechanical (NEM) switches are energy-efficient devices, which transduce current signals by using mechanical deformation created by an electrostatic field. In contrast with electronic switches, whose efficiency is bound by thermionic limit, the operating principle of NEM switches allow them to expend little switching energy while simultaneously maintaining high signal-to-noise ratio. Achieving both benefits simultaneously is made possible by the physical separation of NEM switch components in the OFF state.

The unique advantages of NEM switches have already been demonstrated in low-voltage, low-power and high-temperature applications [1–4]. There is ongoing research concerning the integration of NEM switches into the existing semiconductor electronics platforms (i.e., complementary metal oxide semiconductors or CMOS) [5, 6]. Also in comparison with commercially available microelectromechanical (MEM) systems that are widely found in acceleration sensors and gyroscopes, NEM switches would offer increased speed and miniaturization. Although NEM switches have demonstrated great prospects for high-temperature operation, a gap has been identified in research that concerns NEM switch operation at low temperatures. Demonstration of cryogenic operation would be beneficial for emerging quantum computing device applications [7].

Depending on the size of the building blocks, two main methods of NEM switch fabrication can be distinguished: top-down and bottom-up. One-dimensional (1D, e.g., nanowires) and two-dimensional (2D, e.g., thin films) materials serve as NEM switch active elements, which by deforming make and break mechanical contact with immovable electrodes. The size range of the active elements is from several to a hundred nanometres in thickness and tenths to hundreds of micrometres in length. Nanowires are quasi-1D nanostructures boasting high surface-to-volume ratio, crystallinity, low defect concentration, high resonant frequency and ease of combining materials with different crystalline structures.

For nanowire integration into devices, it is necessary to control and characterize their synthesis yield, and physical and chemical properties. Wide information regarding the properties of nanowires is available in the literature, however, the properties may differ from one synthesis to another. Therefore, characterization of morphological, electrical and mechanical properties is necessary as a result of each synthesis. The preferred approach is to combine different characterization methods to confirm the reliability of the results.

The operating principles of devices based on 1D nanostructures can be conveniently investigated using *in situ* methods inside, for example, scanning

electron microscope (SEM [8, 9]) or transmission electron microscope (TEM [10]). By using nanomanipulators, *in situ* methods allow monitoring of 1D nanostructure deformation in real-time. The distance between the active element and electrode can be adjusted in a wide range, allowing characterization of different deformation regimes and finding the most optimal one for NEM switch operation. One challenge that needs to be addressed to make nanowire-based devices compatible with traditional thin-film processing technologies, is nanowire integration onto a planar substrate with electrodes. The main issues that currently require increased focus are the repeatability of the integration process in terms of yield and nanowire alignment precision.

Integrated nanowire devices are still laboratory-scale endeavours and are not available commercially. The creation of prototypes and characterization of their operation would significantly advance the NEM switch research field towards the implementation of industrial applications.

1.2. Objective and tasks of the thesis

The **objective** of this thesis is investigation of operating principles of bottom-up synthesized one-dimensional semiconductor nanostructure-based NEM switches on-chip for their use at room and cryogenic temperatures.

The **tasks** of this thesis are:

1. To find synthesis parameters that result in optimal nanostructure yield and morphology for NEM switch applications.
2. To determine mechanical and electrical properties of the synthesized 1D nanostructures for application in NEM switches and for creating guidelines for NEM switch fabrication.
3. To find optimal parameters for the operation of a NEM switch by using the determined morphology, electromechanical properties, *in situ* measurements and theoretical model.
4. To fabricate electrode systems for alignment of 1D nanostructures and to investigate nanostructure transfer and alignment methods on-chip.
5. To fabricate NEM switches and to demonstrate their operation at room temperature and cryogenic temperatures.

1.3. Theses to be defended

1. The developed bottom-up growth methods enable obtaining optimal nanostructure yield and morphology for creating integrated nanoelectromechanical switches (publications V and VII).
2. Bottom-up semiconductor nanostructures (CuO and Bi_2Se_3) grown using the controlled synthesis can be integrated into planar nanoelectromechanical switches using transfer and alignment of nanostructures on electrodes, supercritical drying and contact fabrication (publications I, III, IV and VI).

3. Repeatable operation of integrated bottom-up grown one-dimensional nanostructure-based nanoelectromechanical switches is demonstrated at room (with CuO nanowires) and cryogenic (with Bi_2Se_3 nanobelts) temperatures. Current that flows through the Bi_2Se_3 nanobelt during switching, is connected to the deformation of the nanostructure and could be used to control NEM switching (publications I, III and VI).

1.4. Scientific novelty of thesis

This thesis is devoted to applications of bottom-up grown semiconductor nanostructures in nanoelectromechanical (NEM) switches. The most significant findings that may contribute to the development of the general field are the following:

- It is shown for the first time how the diameter of a gold catalyst influences the morphology of Bi_2Se_3 nanobelts.
- A fabrication flow of bottom-up one-dimensional semiconductor nanostructure integration into planar NEM switches is developed.
- Operation of a NEM switch with CuO nanowire as the active element is demonstrated for the first time.
- Operation of a NEM switch with topological insulator Bi_2Se_3 nanobelt as the active element is demonstrated for the first time, paving way for use of topological surface states in NEM switches.
- NEM switch operation at temperatures lower than 77 K is demonstrated for the first time.
- It is demonstrated for the first time how monitoring the current through the nanostructure could be used to control the deformation of the active element during NEM switching.

1.5. Practical significance of thesis

Application of bottom-up grown one-dimensional semiconductor nanostructures holds great promises in the development of such future NEM switches that would offer a wide functionality in various fields including electronics, sensors, material characterization and quantum computing.

The knowledge about CuO and Bi_2Se_3 one-dimensional nanostructure tailored synthesis and electromechanical properties could benefit not only the research and industry fields of nanoelectromechanical switches. The findings described in this thesis are also relevant for the development of flexible electronics, thermoelectrics, electrochemical CO_2 reduction and sensor applications. The integration method developed in this work can be applied for bottom-up grown nanostructures of different materials, as well as for other low-dimensional materials such as graphene and 2D van der Waals materials.

The demonstration of nanoelectromechanical switching at cryogenic temperatures, using Bi_2Se_3 contributes to the development of such NEM switches, that will exploit the unique properties of the topological surface states, particularly their ballistic charge carrier transport for the development of energy-efficient electronic devices. The demonstration of a novel switching mode that exploits current control through the nanostructure could aid in developing more reliable NEM switches.

1.6. Author's contribution

The author contributed to the characterization of synthesis yield of one-dimensional nanostructures, characterization of their mechanical and electrical properties, fabrication of nanoelectromechanical switches, their characterization and operation testing and optimization. The author contributed to experiment planning, conducting experiments, data analysis and summary, contributed to publication writing and editing.

J. Kosmaca (J. K.), R. Meija (R. M.), R. Sondors (R. S.) and M. Antsov contributed to characterization of mechanical properties of nanostructures and J. K., R. M. and R. S. to the creation of NEM switches. R. S. carried out synthesis experiments, J. K. and M. M. Ramma contributed to investigation of CuO dielectrophoresis. G. Kunakova contributed to the electrical characterization of nanostructures. A. I. Livshits developed the theoretical model for calculation of NEM switch-ON voltage, K. Niherysh contributed to NEM switch measurements at low tempertures. J. Prikulis and R. Poplausks contributed to development of the electrical resonant frequency detection system. E. Dzene and E. Kauranens contributed to NEM switch fabrication and characterization. D. Erts contributed to experiment planning and revising publications.

1.7. Approbation of the thesis

Publications included in this thesis

I. Niherysh, K.; Jasulaneca, L.; Dzene, E.; Lombardi, F.; Erts D. Effect of Bending Deformation on Suspended Topological Insulator Nanowires: Towards a Topological Insulator Based NEM Switch. *Sensors and Actuators, A: Physical*, **2024**, *371*, 115292.

II. Jasulaneca, L.; Poplausks, R.; Prikulis, J.; Dzene, E.; Yager, T.; Erts, D. Characterization of Mechanical Oscillations in Bismuth Selenide Nanowires at Low Temperatures. Micromachines **2023**, *14* (10), 1910.

III. Jasulaneca, L.; Meija, R.; Kauranens, E.; Sondors, R.; Andzane, J.; Rimsa, R.; Mozolevskis, G.; Erts, D. Cryogenic Nanoelectromechanical Switch Enabled by Bi_2Se_3 Nanoribbons. *Materials Science and Engineering: B* **2022**, *275*, 115510.

IV. Ramma, M. M.; Katkevics, J.; Jasulaneca, L.; Kunakova, G.; Sondors, R.; Meija, R.; Erts, D.; Kosmaca, J. Dielectrophoretic Alignment and Electrical Characterization of CuO Nanowire-Based Systems. *Surfaces and Interfaces* **2021**, *27*, 101531.

V. Sondors, R.; Kunakova, G.; Jasulaneca, L.; Andzane, J.; Kauranens, E.; Bechelany, M.; Erts, D. High-Yield Growth and Tunable Morphology of Bi_2Se_3 Nanoribbons Synthesized on Thermally Dewetted Au. *Nanomaterials* **2021**, *11* (8), 2020.

VI. Jasulaneca, L.; Livshits, A. I.; Meija, R.; Kosmaca, J.; Sondors, R.; Ramma, M. M.; Jevdokimovs, D.; Prikulis, J.; Erts, D. Fabrication and Characterization of Double- and Single-Clamped CuO Nanowire Based Nanoelectromechanical Switches. *Nanomaterials* **2021**, *11* (1), 117.

VII. Sondors, R.; Kosmaca, J.; Kunakova, G.; Jasulaneca, L.; Ramma, M. M.; Meija, R.; Kauranens, E.; Antsov, M.; Erts, D. Size Distribution, Mechanical and Electrical Properties of Cuo Nanowires Grown by Modified Thermal Oxidation Methods. *Nanomaterials* **2020**, *10* (6), 1051.

VIII. Meija, R.; Livshits, A. I.; Kosmaca, J.; Jasulaneca, L.; Andzane, J.; Biswas, S.; Holmes, J. D.; Erts, D. Resonance Assisted Jump-in Voltage Reduction for Electrostatically Actuated Nanobeam-Based Gateless NEM Switches. *Nanotechnology* **2019**, *30* (38), 385203.

IX. Jasulaneca, L.; Kosmaca, J.; Meija, R.; Andzane, J.; Erts, D. Review: Electrostatically Actuated Nanobeam-Based Nanoelectromechanical Switches – Materials Solutions and Operational Conditions. *Beilstein Journal of Nanotechnology* **2018**, *9* (1), 271–300.

X. Livshits, A. I.; Jasulaneca, L.; Kosmaca, J.; Meija, R.; Holmes, J. D.; Erts, D. Extra Tension at Electrode-Nanowire Adhesive Contacts in Nano-Electromechanical Devices. *European Journal of Mechanics, A/Solids* **2017**, *66*, 412–422.

XI. Kosmaca, J.; Jasulaneca, L.; Meija, R.; Andzane, J.; Romanova, M.; Kunakova, G.; Erts, D. Young's Modulus and Indirect Morphological Analysis of Bi_2Se_3 nanoribbons by Resonance Measurements. *Nanotechnology* **2017**, *28* (32), 325701.

Publications not included in this thesis

XII. Kosmaca, J.; Katkevics, J.; Andzane, J.; Sondors, R.; Jasulaneca, L.; Meija, R.; Niherysh, K.; Rublova, Y.; Erts, D. Humidity-Dependent Electrical Performance of CuO Nanowire Networks Studied by Electrochemical Impedance Spectroscopy. *Beilstein Journal of Nanotechnology* **2023**, *14* (1), 683–691.

XIII. Kosmaca, J.; Jasulaneca, L.; Meija, R.; Sondors, R.; Erts, D. Nanowires for Nems Switches. *NATO Science for Peace and Security Series B: Physics and Biophysics* **2020**, 201–207.

List of selected international conference presentations

1. Jasulaneca, L.; Dzene, E.; Sondors, R.; Prikulis, J.; Erts, D. Bottom-Up Semiconductor 1D Nanostructures for Mechanical Switching. IEEE-NANO 2023: The 23rd IEEE International Conference on Nanotechnology, July 2–5, 2023, Jeju Island, Korea.
2. Dzene, E.; Jasulaneca, L.; Sondors, R.; Prikulis, J.; Niherysh, K.; Erts, D. Suspended Bi_2Se_3 nanostructures for substrate-free magnetoelectric characterization and device applications. IEEE-NANO 2023: The 23rd IEEE Interational Conference on Nanotechnology, July 2–5, 2023, Jeju Island, Korea.
3. Sondors, R.; Kunakova, G.; Andzane, J.; Jasulaneca, L.; Salnajs, D.; Lombardi, F.; Erts, D. Physical Vapor Deposition Synthesis Methods for Bi_2Se_3 NR with Tunable Geometry. 3-day International Conference on Materials Science, October 26–28, 2022, Verona, Italy.
4. Dzene, E.; Jasulaneca, L; Sondors, R.; Erts, D. Comparison of methods for integration of Bi_2Se_3 nanowires in NEM switches. FM&NT-NIBS 2022 conference, July 3–6, 2022, Riga, Latvia.
5. Jasulaneca, L.; Meija, R.; Kauranens, E.; Sondors, R.; Andzane, J.; Prikulis, J.; Dzene, E.; Erts, D. On-chip Bi_2Se_3 nanowire nanoelectromechanical switches for cryogenic switching. ISNTT2021 International Symposium on Novel Materials and Quantum Technologies. Atsugi, Japan, December 14–17, 2021.

2. THEORETICAL OVERVIEW

2.1. Nanoelectromechanical switches

Nanoelectromechanical (NEM) switches are considered perspective components for future electronics due to their unique advantages such as high energy efficiency, temperature and radiation stability, speed and scalability [11–13]. Operation of NEM switches has been demonstrated in memory and logic elements [11].

Electrical and mechanical interaction between the active element and the electrode of the NEM switch allows to implement ON and OFF states (fig. 2.1) [10, 14]. No force is applied between the active element and the electrode in the OFF state, and they are separated from each other at a distance z_0. Thus the electrical circuit is open, and the current through it is near zero. When voltage is applied between the active element and the electrode, electrostatic force F_{el} starts to act in a direction opposite to the elastic force F_{elas} and deforms the active element towards the electrode. When the instability point is reached, the active element accelerates rapidly and establishes contact with the electrode. This manifests as a high current jump in the circuit. By decreasing the voltage, F_{elas} acts against two forces: adhesion force between the active element and the electrode F_{adh} and F_{el}. As soon as F_{elas} is larger than sum of F_{adh} and F_{el}, the active element returns to the starting point.

Two most popular NEM switch configurations are two-terminal (2T fig. 2.1 (a)) [15] and three-terminal (3T, fig. 2.1 (b)) [16]. In a 2T configuration, the active element is grounded (source, S) and immovable electrode (gate, G) serves both the actuation and transduction functions. In a 3T switch

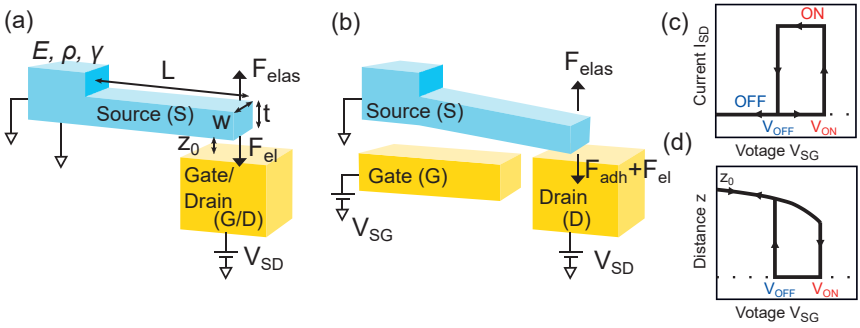

Figure 2.1. **Schematics of NEM switch configurations (single-clamped). (a) Two-terminal switch in OFF state and (b) three-terminal switch in ON state. Young's modulus E, density ρ and surface energy γ are the main material parameters, that govern the operation of the switch. (c) Typical NEM switch operation I-V characteristics. (d) Distance as a function of voltage applied between the active element and the electrode during switching**

the actuation electrode (G) is separated from the transduction electrode (drain, D) at a slightly larger distance from the active element. Due to the larger distance, the operating voltage of 3T switch is increased in comparison with 2T, however, the independent operating voltage control serves as an important advantage. NEM switches can be configured to operate with single-clamped and double-clamped active elements.

In the simplest model a double-clamped NEM switch can be described as a parallel plate condenser with one movable plate, and its corresponding switching-ON voltage can be expressed as [17]

$$V_{ON} = \sqrt{\frac{8kz_0^3}{27\varepsilon_0 A}} \tag{2.1}$$

2.2. One-dimensional nanostructures

Thanks to the atomically smooth surface, crystallinity, tunable electrical properties and possibility for easy selective doping that allows to combine vastly different materials, quasi-one-dimensional nanostructures have become perspective candidates for future electronic devices [18]. Their application in NEM switches would increase their operating speed, decrease size and endow them with extra functionality.

In this thesis semiconductor Ge, CuO and Bi_2Se_3 one-dimensional nanostructures were used as NEM switch active elements.

CuO is a p-type semiconductor with band gap of 1.2 eV [19] and monoclinic crystal structure. CuO nanowires have gained attention in such applications as chemical and gas sensors [20] and have also been demonstrated as a channel material in a field effect transistor [21]. Thanks to its high melting temperature of 1326 °C [22], CuO nanowires are perspective for high temperature NEM switch applications. CuO nanowires can be grown with high yield using simple synthesis methods such as thermal Cu oxidation [23]. Nanowire morphology can be controlled by using external electric field [24] and humidity [25].

Bi_2Se_3 is a semiconductor with band gap of 0.3 eV, it has rhombohedral crystal structure [26]. Its structure is layered, consisting of in-plane atoms with covalent bonding, and van der Waals bonding between these planes [27]. In crystallographic c-axis direction Bi_2Se_3 is theoretically an insulator in the bulk and has conducting 2D surface states, which is a characteristic of 3D topological insulator (TI) material class [26]. To observe topological surface states, Fermi level has to lie in the band gap [28]. This is a challenge for Bi_2Se_3 as it contains natural Se vacancies [29] that move the Fermi level to the conduction band. Due to their high surface-volume ratio nanostructures are well suited platforms for reducing bulk charge carrier contribution to the total conduction and thus for observing surface states [30]. Mechanical deformation is another means of controlling the band structure of TI materials [31–33], propelling the investigation of these materials in NEM switches.

Ge nanowires possess high Young's modulus (100–150 GPa) and high strength [34], making them suitable for switching in 2T NEM switch configuration. Repeatable NEM switching has been demonstrated with Ge nanowires *in situ* inside scanning electron microscope (SEM) [8, 9]. Native oxide layer, that forms on Ge surface in air ambient, functions as a tunnel barrier [9, 10, 35], which increases the energy necessary for electron injection from the metallic contacts. Therefore, at low voltages Ge nanowire-based NEM switches exhibit high resistance and low current. At the same time, the presence of the oxide layer decreases the risk of Ge nanowire degradation during the current jump. For synthesis of Ge nanowires, both liquid and vapor phase methods have been used. The highest synthesis yield up to 80 % has been reported using supercritical fluid synthesis [36].

2.3. Integrated NEM switches

In situ investigation of NEM switches inside transmission and scanning electron microscopes [8–10] has significantly expanded the understanding of their operational principles. *In situ* research allows following the dynamic processes occurring in the NEM switch in real time, providing information about material and contact properties. Another benefit of *in situ* measurements is the ease of creating different active element-electrode configurations. Therefore, *in situ* measurements are an important step in the process of fabricating integrated NEM switches – after the principle has been verified, an integrated device with lower reconfigurability but higher stability can be fabricated.

Fabrication and characterization of integrated NEM switches on planar substrates is a many-step process (fig. 2.2), which embraces synthesis of nanomaterials and characterization of their size distribution (fig. 2.2 (a)), characterization of their mechanical and electrical properties, and investigation of integration methods (fig. 2.2 (b)), and finally, short and long-term testing of NEM switch operation in different environments (fig. 2.2 (c)).

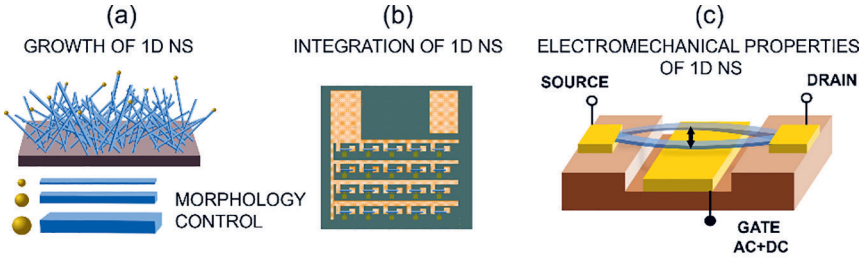

Figure 2.2. **Development and characterization of an integrated NEM switch. (a) Growth and morphology control of one-dimensional nanostructures. (b) Fabrication of electrode systems and alignment of one-dimensional nanostructures and contact formation on top of the nanostructures. (c) Schematics of integrated NEM switch characterization**

3. MATERIALS AND METHODS

3.1. Synthesis of one-dimensional nanostructures

CuO and Bi_2Se_3 one-dimensional nanostructures were synthesized using thermal oxidation and physical vapor deposition in a quartz tube vacuum furnace at the Institute of Chemical Physics, University of Latvia. CuO nanowires were grown on a 25 μm thick Cu foil (99.9% purity, Goodfellow GmbH). One oxidation cycle consisted of raising the temperature with rate of 16 °C/min up to 500 °C and the oxidation was carried out for 210 min at constant temperature of 500 °C. Then the furnace was allowed to cool down to room temperature.

Au catalyst nanoparticles with diameters 8–150 nm were obtained by heating thermally evaporated Au thin films with thickness 1.5–16 nm on a glass substrate.

Bi_2Se_3 nanostructures were grown from Bi_2Se_3 powder (99.999% purity Bi_2Se_3 powder, Sigma-Aldrich) on glass substrate in nitrogen atmosphere using both catalyst-assisted and catalyst-free process. Before heating, the furnace tube was purged with N_2 gas. During one growth cycle, the temperature was raised to 585 °C in 45 minutes, then kept constant for 15 minutes, and lowered to 535 °C. In this part of the cycle, Bi_2Se_3 evaporation was taking place. At the next stage, N_2 flow at a constant pressure of 25 Torr was used to initiate 1D NS growth. As the temperature reached 500 °C, the flow was stopped and at 475 °C the pumping was also stopped. To complete the process, the tube was filled with N_2 and the substrate was removed when the temperature was in the range of 110–170 °C.

Germanium (Ge) nanowires were synthesized using supercritical fluid method (SCF) at University College Cork (Cork, Ireland).

3.2. Characterization of mechanical, charge carrier transport and contact properties of one-dimensional nanostructures

The morphology of one-dimensional nanostructures was characterized using scanning electron microscope (SEM, Hitachi FE-SEM S 4800) and atomic force microscope (AFM, Asylum Research MFP-3D). SEM was used to determine length, width and thickness of 1D NS. To determine size of a single 1D NS in SEM, it was attached to an etched Au electrode tip and rotated using a micromotor (Faulhaber ADM0620) to find the longest and shortest projections.

AFM was used to determine thickness and shape of 1D NS, as well as the deformation profiles of suspended 1D NS. AFM was used in dynamic oscillation regime, to minimize the effect of shear force that could result in sliding or deformation of the suspended nanostructure. Cantilevers with resonant

frequency 300 ± 100 kHz and force constant 8.4–57 N/m (AC160TS) were used.

Mechanical properties were determined in the elastic regime using quasi-static and dynamic methods of deformation. The quasi-static approach involved a 1D NS that was fixed in two points and a gradually increasing force was applied to its middle point by an AFM tip, simultaneously measuring the force and deformation. The dynamic method involved inducing vibrations in the 1D NS by application of an alternating voltage combined with direct voltage. The vibrations were detected visually in SEM and electrically using a vector network analyzer (VNA, Rohde & Schwarz ZNB 8). The fundamental resonant frequency was determined as the frequency where the vibration amplitude was maximum and whose amplitude dependence could be described by a Lorentz function. Fundamental resonant frequency and dimensions of the 1D NS were employed to calculate Young's modulus. To determine mechanical vibration dependence on temperature for Bi_2Se_3 nanobelts, an electrical system for signal amplification in PPMS was created.

Charge carrier transport was measured in two-probe and four-probe configurations, fabricating metal thin-film electrodes on top of the 1D NS. Temperature-dependent resistance was characterized for Bi_2Se_3 nanobelts in a physical property measurement system (PPMS, DynaCool 9T, Quantum Design) in a temperature range from 300 to 2 K. Magnetoresistance of Bi_2Se_3 nanobelts was characterized at low temperatures in perpendicular magnetic field up to 14 T. Field-effect was characterized by measuring longitudinal resistance $R_{S\text{-}D}$ as a function of gate voltage through SiO_2 dielectric.

3.3. Fabrication and characterization of a NEM switch

In this work, integrated NEM switches were fabricated in two configurations. For NEM switches with bottom contacts, the active element was fixed to the thin film electrode underneath by the adhesion force. NEM switches with top contacts employed additional thin film electrodes covering the ends of the active element for improved electrical and mechanical stability.

Si chips with resistivity 1–50000 Ω·cm with a thin film of thermal SiO_2 with a thickness of 200 to 1000 nm were used as substrates.

Thin-film electrodes (S, D and G) were fabricated using photo- and electron beam lithography (EBL). Photolithographic patterning employed direct write laser lithography (Heidelberg μPG 101 Tabletop Micro Pattern Generator) and mask aligner tools (Mask aligner Suss MA/BA6 Gen4). EBL (Raith eLINE) was used to fabricate electrodes that are narrower than 1 μm. G electrodes were fabricated into trenches, created by wet and dry etching methods. For the metallization of electrodes, a 5 nm Ti adhesion layer and 55–195 nm Au thermal evaporation were thermally evaporated. The excess metal was removed by dissolving the undeveloped resist.

1D NS were transferred on substrates with the as-fabricated electrodes by using mechanical transfer, dielectrophoresis and nanomanipulations in SEM. To reduce contact resistance, the native oxide of Bi_2Se_3 nanobelts was etched before top-contact metallization. Finally, NEM switches were dried in supercritical CO_2 to minimize risks for 1D NS stiction to the G electrode under the influence of capillary forces.

3.4. Characterization of NEM switch operation

Operation of NEM switches was characterized *in situ* inside SEM at room temperature and in PPMS at cryogenic temperatures as low as 2 K. For measurements *in situ,* a nanomanipulation system (SmarAct 13D) with 4 3D nanomanipulators was used to adjust the distance between the electrodes and to apply external force. In contrast to the integrated on-chip NEM switch, the active elements were not fixed to planar substrates but on sharp etched tips of gold electrodes. The same electrodes and gold-coated AFM cantilevers were used as stationary electrodes.

The electrostatic force was applied in two ways to characterize NEM switch operation, as shown in fig. 3.1. To determine precise V_{ON} and V_{OFF} values and to investigate their evolution during switching, gate voltage G was swept gradually using small voltage steps. The second approach was used to measure ON and OFF-state current evolution during extended switching. Here, a periodical square voltage pulse was applied between S and G electrodes, while simultaneously measuring the current level that corresponds to each voltage. In this case, precise information about V_{ON} and V_{OFF} is not available, however, the time over which the current flows through the active element is reduced thus minimizing risks of modification of contact properties.

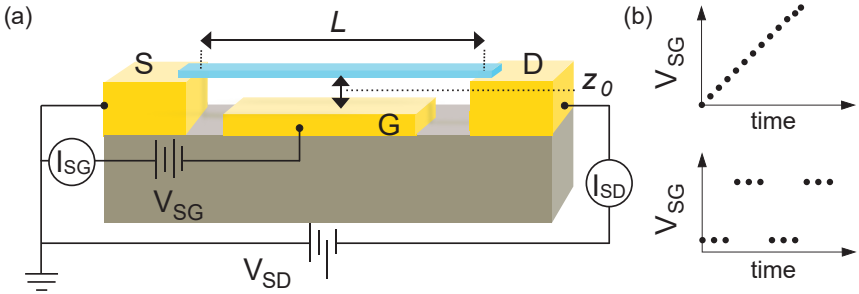

Figure 3.1. **Operation of integrated 1D NS-based switches. (a) Schematics of electrical connections and terminal designations for NEM switch operation testing. (b) Top: Sweeping of V_{SG} to precisely determine V_{ON} and its evolution; Bottom: Square V_{SG} signal to observe time evolution of I_{ON} and I_{OFF}**

Two distinct switching control modes were investigated: with and without current control before the formation of the contact between the active element (S) and the lower (G/D) electrode. In a conventional 2T NEM switch, as the voltage between S and G electrodes slowly increases, changes in S-G current are usually first detected at the moment of contact establishment. The second mode employed all 3 terminals: S-D current was registered before contact formation as a function of deformation of the active element, while S-G current signalled the establishment of the contact.

4. RESULTS AND DISCUSSION

4.1. Synthesis of one-dimensional nanostructures

CuO nanowires grown by thermal oxidation were found to be cylindrical with diameters ranging from 20 to 320 nm. Thermal oxidation with an electric field and increased humidity produced nanowires with yield and size distribution that is the most appropriate for NEM switch fabrication. The as-described synthesis resulted in nanowires on the cathode side with a mean diameter of approximately 70 nm, a mean length of approximately 5 μm and a high length-to-diameter ratio.

Annealing of 3 nm thin Au catalyst thin-film was used to produce Au nanoparticles with a mean diameter of 10 nm. Synthesis on these nanoparticles resulted in the highest yield of Bi_2Se_3 nanobelts of approximately 100 nanobelts per 1000 μm^2. The obtained synthesis yield exceeded the previously obtained yield using catalyst-free synthesis by almost 50 times [37]. The catalyst-assisted method allowed to tune the mean length of Bi_2Se_3 nanobelts in the range from approximately 3 to 6 μm and the mean thickness from 30 to 110 nm. For a double-clamped NEM switch with a typical trench depth of 200 nm, these dimensions would lead to an estimate of V_{ON} in the range from 13 V to 32 V, and resonant frequencies from 7.5 MHz to 8.2 MHz.

4.2. Mechanical and transport properties of one-dimensional nanostructures

4.2.1. Mechanical properties

Young's modulus of CuO and Bi_2Se_3 1D NS was determined, using *in situ* SEM resonance method complemented with three-point bending tests by AFM for CuO.

For cylindrical-shaped CuO nanowires obtained by thermal oxidation, a size dependence of Young's modulus on nanowire diameter was observed (fig. 4.1. (a)). For a diameter range from 20 to 160 nm the change of E could be described by an exponential function, tending to 95 GPa for large values of d. This is close to Young's modulus value for macroscopic CuO of 82 GPa [38]. A prominent size dependence of Young's modulus was determined for nanowires with a diameter smaller than 50 nm, reaching a value as large as 550 GPa. This effect was more pronounced in bending deformation than in resonance. The different trends obtained for both methods could be explained by different boundary conditions at the nanowire ends. In the case of resonance, the nanowire was clamped at one end, while in the case of bending – at both ends, increasing the possibility of developing intrinsic mechanical stresses.

A similar size dependence has been reported for CuO nanowires in literature, using three-point bending deformation [38]. In the diameter range from 190 nm to 80 nm an approximately three-fold increase in Young's modulus value has been observed. However, the smallest diameter of the studied nanowires was 80 nm [38], while in this thesis it is approximately 20 nm. In general, the size dependence of Young's modulus can be explained by surface strain, which in case of decreasing size gives a larger contribution to the total elasticity [39].

The number of fundamental resonant frequencies depends on the cross-section of the 1D NS. In contrast to CuO, whose cylindrical symmetry led to the existence of only one resonant frequency, Bi_2Se_3 nanobelts with their rectangular cross-section exhibited two mutually orthogonal fundamental resonant frequencies. One was in the width w direction (f_w), while the other was in the thickness t direction (f_t). For an ideal rectangle, the ratio of these frequencies should coincide with the ratio of width to thickness. However, for Bi_2Se_3 discrepancies from this ratio were observed. These discrepancies could be explained by the particular morphology of the Bi_2Se_3 surface – as Bi_2Se_3 is a layered material, step-like terraces tend to develop on its surface during the synthesis process [37, 40]. These terraces impact the cross-sectional area and area moment of inertia and thus need to be considered when calculating the value of E. The presence of terraces could be most precisely confirmed using AFM, however, that was a time-consuming process, that involved nanowire transfer on a flat substrate. Therefore, a method was developed that allows the distinguishing of nanobelts with ideally rectangular cross-sections from nanobelts with terraced morphology using resonance.

A parameter k was introduced to describe to what extent a given cross-section deviates from a rectangular:

$$k = \frac{f_t/f_w}{t/w} \tag{4.1}$$

Using parameter k, the experimental results were divided into 2 groups. Only nanowires with rectangular cross-sections were used for the determination of Young's modulus (fig.4.1. (b) filled data points).

Fig. 4.1 (b) shows dependence of resonant frequency parameters F_t and F_w on nanobelt thickness and width. The observed linear relationship indicates that Young's modulus does not depend on the cross-sectional size. The slope of the line is proportional to $\sqrt{(E/\rho)}$, where ρ – Bi_2Se_3 mass density (7680 kg m^{-3} [41]). E was calculated using the following expressions for resonant frequency parameters:

$$F_t = t\sqrt{\frac{E}{\rho}} \text{ and } F_w = w\sqrt{\frac{E}{\rho}}, \tag{4.2}$$

where

$$F_t = \frac{4\sqrt{3}\pi f_t L^2}{\beta^2} \text{ and } F_w = \frac{4\sqrt{3}\pi f_w L^2}{\beta^2}. \tag{4.3}$$

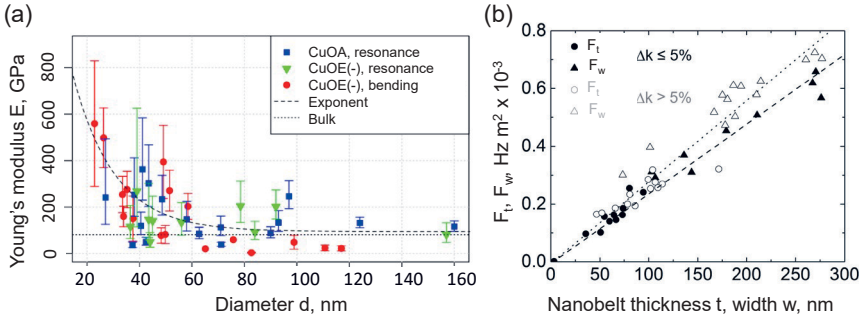

Figure 4.1. **Young's modulus of CuO un Bi_2Se_3 1D NS determined using resonance and AFM three-point bending. (a) Diameter-dependent E of CuO nanowires. Experimental points denote nanowires grown on the anode (CuOA) and cathode (CuOE-) side, dashed trendline – approximation with an exponent, solid line – Young's modulus of macroscopic CuO. (b) Frequency parameters obtained using the resonance method as a function of nanobelt thickness and width. Filled data markers denote nanobelts with rectangular cross-sections, empty – terraced nanobelts**

In eq. (4.3), L is the length of the nanobelt and β = 1.875 – a constant, derived from the equation for a fundamental resonant frequency of a single-clamped beam. The value of the slope value was found to be 2.4 ± 0.1 × 10^3 m s^{-1} and the corresponding average value of Young's modulus was 44 ± 4 GPa. This value is nearly the same as that of the macroscopic Bi_2Se_3 crystal (47 ± 9 GPa [42]), which may be attributed to a similar defect density in the as-grown nanobelts. Fig. 4.1 (b) also shows a 30% increase in Young's modulus when terraced nanobelts are included in the calculation, which could be explained by a larger surface area and a higher contribution from surface effects.

Investigation of mechanical properties of double-clamped nanostructures using AFM is a reliable, but time-consuming method. It is also limited to room-temperature measurements. To measure the temperature-dependence of dynamic mechanical properties in double-clamped NEM switches, an electrical system for resonant frequency read-out that is compatible with PPMS was developed. The principle of electrical detection was based on the fact, that mechanical vibrations in semiconductor nanowires influence also the current flowing through the nanowire [43, 44]. The resonance can then be detected by measuring the changes in the transmission coefficient S_{21} of the signal that induces the vibrations.

Fig. 4.2 shows the results obtained with the developed read-out system for a double-clamped Bi_2Se_3 nanobelt with a length of 7.6 μm, width of 224 nm, thickness of 125 nm and S-D resistance of 50 Ω (fig. 4.2 (a)). The amplitude response of parameter S_{21} exhibits an asymmetrical peak near 1.5 MHz frequency (fig. 4.2 (b)). This peak was attributed to the mechanical resonance of the nanobelt. To verify this assumption, the nanobelt was replaced with a 20 Ω resistance (with a value close to the S-D resistance of the nanobelt). In this case,

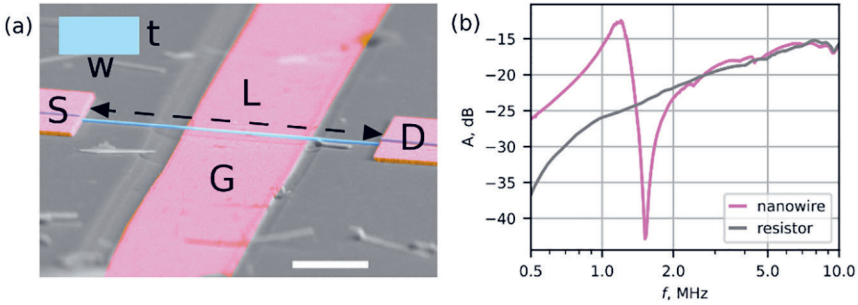

Figure 4.2. **Electrical read-out of Bi_2Se_3 nanobelt resonant frequency. (a) Angled-view false-color SEM image of Bi_2Se_3 resonator showing the suspended nanobelt and S, D and G electrodes. The nanobelt is suspended approximately 200 nm above the G electrode and under S and D electrodes. Scale bar is 2 μm. (b) S21 parameter amplitude spectrum shows an asymmetric peak near 1.5 MHz for Bi_2Se_3 nanobelt (magenta curve). For comparison, the amplitude spectrum for a 20 Ω resistor in the circuit shows no peak (grey curve)**

no peak was determined in the amplitude-frequency spectrum of the system, as indicated by the grey curve in fig. 4.2 (b). When measuring system amplitude dependence on G voltage, only the 1.5 MHz peak showed systematic amplitude changes, while the other spectral regions showed small random changes. These results further confirm that the origin of the asymmetric peak can be attributed to the mechanical vibration of the gateable nanowire.

Vibration dependence on temperature in the range from 5 K to 300 K was characterized for a single Bi_2Se_3 nanobelt with a length of 8.3 μm, thickness of 35 nm and width of 266 nm, and two-terminal resistance of 36 Ω (fig. 4.3.).

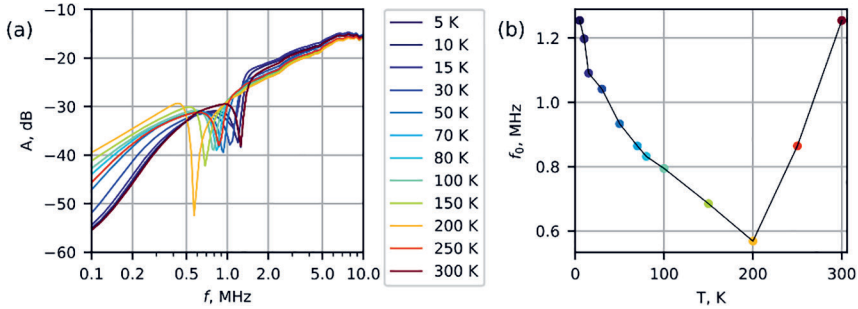

Figure 4.3. **Vibration dependence on temperature for a Bi_2Se_3 nanobelt. (a) S_{21} amplitude parameter for a Bi_2Se_3 nanobelt as a function of temperature in range 5–300 K. (b) Dependence of negative peak frequency f_0 on temperature shows more than a twofold decrease of resonant frequency when the temperature is increased from 5 K to 200 K**

Upon increasing the temperature, the resonant frequency dropped by approximately twice of its initial value, until it reached a minimum at 200 K. As the temperature increased further, the resonant frequency returned to its initial low-temperature value. The same trend was observed in repeated measurements of this sample. The temperature-dependent resonant frequency can likely be explained by fabrication-induced internal stresses in the nanobelt, combined with material differential thermal expansion during heating/cooling [45]. Additional tests would be necessary to fully characterize the deformation of Bi_2Se_3, SiO_2 substrate and Au thin film contacts as a function of temperature.

4.2.2. Charge carrier transport properties

CuO nanowires

CuO nanowires with thermally evaporated top Pd/Au contacts exhibited high scatter in electrical resistivity, with the largest value reaching 540 MΩ. These results indicate that for fabrication of CuO nanowire-based NEM switches with high ON/OFF current ratio, contact optimization should be carried out by, e.g., etching of the nanowire surface and choosing contact metals with tuned work functions. Without optimization, CuO nanowires could serve as robust switching elements for high voltage applications.

Bi_2Se_3 nanobelts

To reduce the contact resistance in Bi_2Se_3-metal top contacts, the native oxide layer covering the nanobelts was etched in a mixture of HCl and CH_3COOH before metallization. Thermal evaporation was carried out immediately after etching under pressure not higher than $7{\cdot}10^{-7}$ mbar. The optimization allowed decreasing the contact resistance of nanobelts by several orders of magnitude and obtaining ohmic I-V characteristics (fig. 4.4 (a-b)). The determined resistivity both for supported on the surface and suspended Bi_2Se_3 nanobelts was on the order of $2–4{\cdot}10^{-5}$ Ω·m at room temperature, which is close to values given in the literature [30]. Fig. 4.4 (c) shows sheet resistance $R_{sheet} = Rw/L$ of a suspended Bi_2Se_3 nanobelt as a function of temperature, where w – width of the nanobelt, L – distance between contacts. For most of the measured samples, a linearly decreasing resistance was observed in the temperature region from 300 K to 20 K. This is a characteristic of Bi_2Se_3 and is usually attributed to its high concentration of native defects in form of selenium (Se) vacancies. For temperatures lower than 20 K, R_{sheet} exhibited saturation (samples with 60 nm and 61 nm thickness in fig.4.4 (c)) or a slight increase (sample with 93 nm thickness in fig. 4.4 (c)). The saturation in the low-temperature region could be explained by the bulk carrier freeze-out mechanism [46], while the increase – with the influence of electron-electron interaction [47, 48].

To confirm the majority carrier type in Bi_2Se_3 nanobelts, field-effect measurements were carried out on a substrate with a SiO_2 dielectric as the gate

oxide and Si as the gate electrode. Changes in resistance $R_{S\text{-}D}$ was monitored while gradually changing gate voltage $V_{S\text{-}G}$ from 0 V to negative and positive polarity at 2 K temperature. Fig. 4.4 (d) shows $R_{S\text{-}D}$ increase in the negative gate voltage range from approximately 17.5 kΩ at 0 V to 18.0 kΩ at –120 V. No $R_{S\text{-}D}$ dependence on gate voltage was registered for gate voltage with positive polarity. These $R_{S\text{-}D}$ field-effect characteristics were attributed to n-type semiconductor behaviour, which could well be explained by the high concentration of negative Se vacancies (in-plane 10^{13}–10^{14} cm^{-2} [29]) in Bi_2Se_3, supporting the trend observed in $R_{S\text{-}D}$ temperature dependence. For lower surface charge carrier concentrations, $R_{S\text{-}D}$ would be expected to reach a maximum value (charge neutrality point) and then decrease with continuously decreasing gate voltage, thus demonstrating ambipolar transport. However, the relatively large nanobelt thickness of 60 nm means that the bulk charge carriers also contribute to the overall charge transport. Together with an accumulation layer that forms at the nanobelt-SiO_2 interface, both extra conduction channels make it more difficult to reach the charge neutrality point.

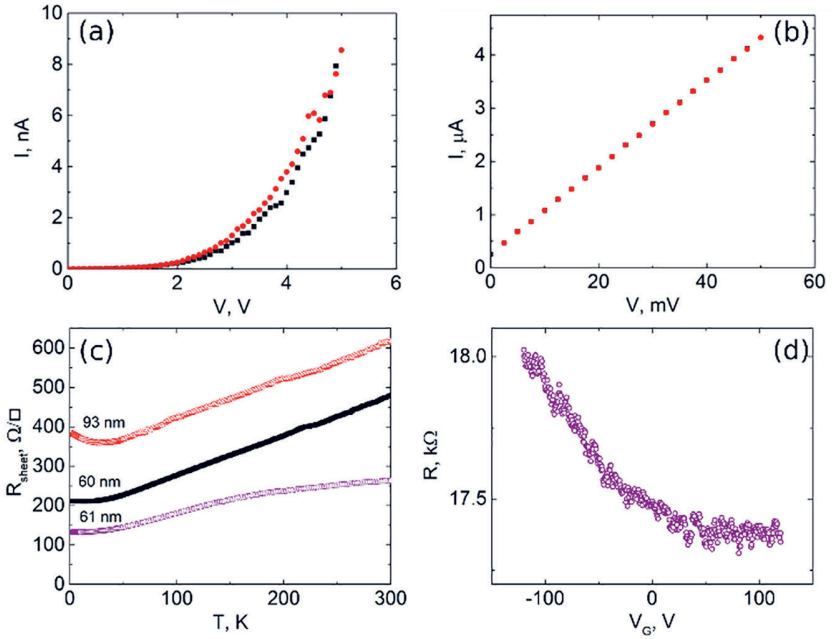

Figure 4.4. **Contact optimization and charge transport properties of Bi_2Se_3 nanobelts. Contact optimization using wet etching allowed to change I-V characteristics from non-linear with high resistance (a) to linear with low resistance (b). (c) Temperature dependence of sheet resistance for 3 suspended nanobelts with different thicknesses in temperature range from 300 K to 2 K. (d) Resistance dependence on gate voltage at 2 K points to n-type majority charge carrier field-effect**

4.2.3. Magnetoresistance measurements

Magnetoresistance (MR) measurements were conducted on both supported and suspended Bi_2Se_3 nanobelts in a perpendicular magnetic field B up to 14 T. Fig. 4.5 (a) displays the characteristic magnetic field dependence of longitudinal resistance R_{xx} for a suspended nanobelt. As the intensity of the magnetic field increases, the resistance also increases, as electrons undergo cyclotron motion due to the Lorentz force, leading to a shortened mean free path. For the majority of the samples, a pronounced negative peak in resistance was observed near B = 0 for small values of B, which is a characteristic of weak anti-localization (WAL) effect (fig. 4.5 (a) and (b)). By measuring WAL dependence on temperature in a range from 2 K to 20 K, diminishing of the peak amplitude was observed at higher temperatures (illustrated as conductance peak dependence on temperature in fig. 4.5 (b)). This decrease could be explained by increased phonon scattering and subsequent reduction of the quantum interference effects. By applying symmetrization to the conductance data and approximating with Hikami-Larkin-Nagaoka's equation [49], electron phase coherence length L_φ dependence on temperature was obtained (fig. 4.5 (c)). Electron phase coherence length at 2 K was approximately 0.7 μm and decreased to 0.1 μm at 20 K. The determined L_φ value for suspended nanobelts at 2 K corresponded to values reported in the literature for a 20 nm thin Bi_2Se_3 film grown by molecular beam epitaxy (MBE) on sapphire substrate at 2 K temperature [50]. This indicates a high quality of the as-grown nanobelts synthesized in this work. Using L_φ dependence on temperature, an exponential factor of –0.62 was obtained. This value is close to –0.5 which is characteristic for 2D systems where the dominant mechanism of decoherence is electron-electron interaction [50].

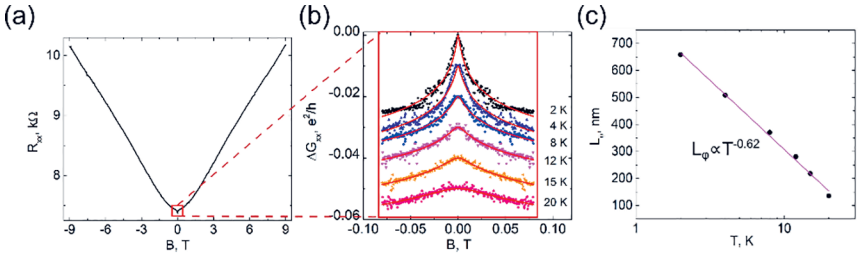

Figure 4.5. **Magnetoresistance measurements for a suspended Bi_2Se_3 nanobelt. (a) Resistance dependence on perpendicular magnetic field of 0–9 T at 2 K. The region of weak anti-localization effect near B = 0 is marked with a red frame. (b) Magnetoresistance curves for sample in (a) are shown as conductance difference G(B)-G(0) in the temperature range of 2–20 K. Solid curves show approximation with Hikami-Larkin-Nagaoka's equation for the WAL effect. (c) Electron phase coherence length Lφ, extracted from the equation, is shown as a function of temperature with an exponential factor of –0.62**

To exclude the impact of sample-to-sample variation of charge carrier properties, MR was characterized for a single Bi_2Se_3 nanobelt, containing both suspended and supported parts (fig. 4.6). Fig. 4.6. (a) shows relative MR, determined as (R(B)-R(0)/R(0) with slightly higher values for the suspended part of the nanobelt. To analyze Shubnikov–de Haas (SdH) oscillations in large magnetic fields, a polynomial background was subtracted from the experimentally obtained R(B) data, and the result was plotted from 4 T to 14 T. Then ΔR was plotted as a function of inverse magnetic field 1/B and its derivative $\partial^2\Delta R/\partial B^2$ analyzed using Fourier transform (fig. 4.6 (b-c)).

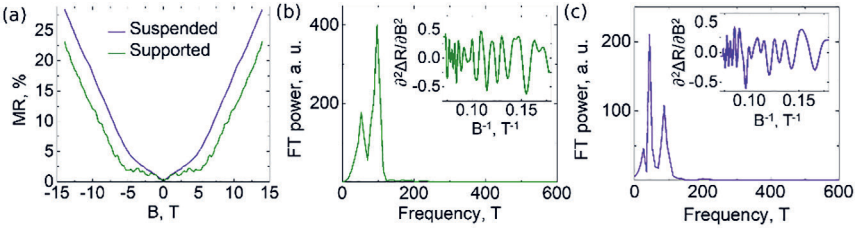

Figure 4.6. **Comparison of magnetoresistance measurements for supported (green curve) and suspended (violet curve) parts of the same Bi_2Se_3 nanobelt in 0–14 T perpendicular magnetic field. Analysis of magnetoresistance data (a) allowed identification of Shubnikov–de Haas oscillations at large magnetic fields (b–c) and extraction of the corresponding characteristic frequencies using Fourier transform. Fourier transformation spectra for double derivative $\partial^2\Delta R/\partial B^2$ (inset) are shown for the supported (b) and the suspended (c) part, respectively**

Two frequencies were identified for the supported part of the nanobelt $F_{supp,1}$ = 52.9 T and $F_{supp,2}$ = 96.9 T. Each of the frequencies extracted from SdH oscillations corresponds to a different conductance channel – bulk, bottom or top surface of the Bi_2Se_3 nanobelt. Charge carrier mobility which is directly proportional to scattering time will determine, how pronounced the oscillations will be in each of the channels. The bottom surface is typically expected to have lower mobility due to the accumulation layer on top of the substrate surface [30]. Therefore, the $F_{supp,1}$ and $F_{supp,2}$ obtained in our study were also attributed to the top surface and bulk states of the supported Bi_2Se_3 part.

As for the suspended part of the nanobelt, three dominating frequencies were extracted: $F_{susp,1}$ = 25.9 T, $F_{susp,2}$ = 43.4 T and $F_{suspp,3}$ = 93.6 T (fig. 4.6 (c)). The lowest frequency $F_{susp,1}$ was attributed to states of the bottom surface, whose mobility is no longer affected by the accumulation layer of the substrate. This means that in a suspended nanobelt both surface conduction channels can be accessed, and NEM switches could serve as a platform for more efficient exploitation of the properties of the surface. A similar three-frequency pattern was observed for suspended Bi_2Se_3 nanowires in [33].

4.3. *In situ* characterization of NEM switches

In situ nanomanipulation methods are used due to the facile reconfigurability they offer – during a single experiment it is possible to explore a vast parameter space by changing distances and angles between the elements. It is particularly important for nanostructures, as they often exhibit scatter in values of various physical properties and *in situ* measurements allow characterization to be conducted on the same sample. The following aspects of NEM switch operation were explored *in situ* inside SEM: how forces in contact may be inferred from the nanowire deformation and how resonance may be applied to decrease the switch-ON voltage and thus minimize risks for nanostructure degradation.

4.3.1. Forces in a NEM switch contact

To determine forces that act in the NEM switch contact, an experiment was carried out consisting of following steps (fig. 4.7 (a-b)): 1) the single-clamped active element (NW) with length L_0 was brought in contact with a plane electrode (G) from a set initial distance L_0h by gradually increasing the gate voltage $V_{S\text{-}G}$; 2) after contact establishment, the experimentally obtained deformation profile of the nanowire was compared with theoretical model, using reaction force components parallel (f_x) and perpendicular (f_y) to the surface; 3) the previous steps were repeated for a different initial distance. The theoretical model was based on Euler-Bernoulli deformation analysis for a non-linear general case, considering the surface reaction force and bending moment M at the point of contact. A typical deformation profile of a single-clamped Ge nanowire with length of 139 μm and radius of 99 nm is shown in fig. 4.7 (b). Deformation profiles were obtained by subtracting SEM images before and after contact establishment. The experimental results were fitted with a theoretical model by choosing the most suitable values for bending moment M and static friction f_x at the contact point.

Fig. 4.7 (c-d) shows the extracted f_y and f_x force components as a function of non-dimensional parameter $|h|$, which corresponds to nanowire deformation and length ratio. f_x values exhibited a large scatter (fig. 4.7 (c)), and their absolute value was comparable to or even exceeded f_y (fig. 4.7 (d)). The obtained results were explained with the dynamics of contact formation in a NEM switch. During pull-in, the free end of the nanowire gets accelerated towards the electrode, and after establishment of a mechanical contact, it continues sliding on the electrode surface. After coming to rest, surface adhesion forces prevent it from returning to its relaxed state, therefore both bending and axial tension deformation acts on a nanowire in a NEM switch contact. A similar analysis could be applied for characterization of double-clamped NEM switch active elements, however, the analyzation of the deformation profiles in SEM would be more complicated.

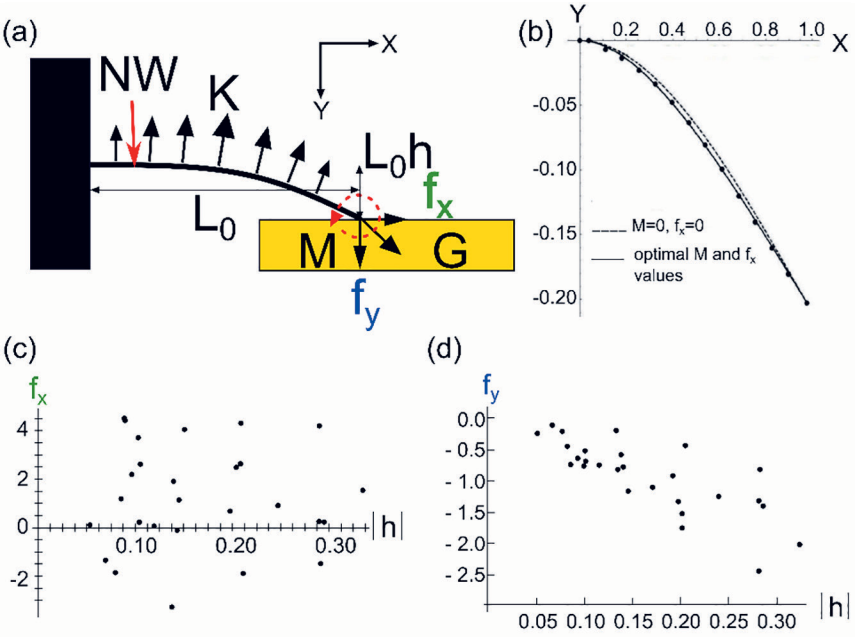

Figure 4.7. **Determination of forces acting in a single-clamped NEM switch contact. (a) Experimental schematics, K – linear density of external applied electrostatic force. (b) Typical deformation profile of a nanowire in contact, where X and Y – coordinates in the direction parallel and perpendicular to the nanowire axis, respectively. Circles mark experimental data points, the dashed line corresponds to the analytical solution at $f_x = 0$ and M = 0 and the solid line – fitted solution using optimal f_x and M values for $|h| = 0.21$. (c) Force component parallel to the surface f_x and (d) perpendicular to the surface f_y as a function of non-dimensional deformation |h|**

4.3.2. Reduction of switching-ON voltage in NEM switches

The operating voltage of the NEM switch is determined by switch-ON and switch-OFF voltages. Reduction of switch-ON voltage would increase the efficiency of the switch and decrease the active element degradation risks. The simplest approach for reducing the V_{ON} in a 2T switch would be to decrease the distance between the active element and the gate. However, smaller distance leads to a smaller elastic force, that may result in insufficient force for returning to the initial OFF-state.

A method for decreasing the operating voltage without compromising the elastic force was developed and experimentally verified. The method involved adding an alternating voltage with frequency close to the fundamental resonant frequency of the nanowire to the conventional direct voltage used for actuation.

In this way the active element undergoes simultaneous quasistatic deformation and dynamically induced deformation.

Reduction of V_{ON} using dynamic actuation was verified using $Ge_{1-x}Sn_x$ nanowire and Bi_2Se_3 nanobelt-based single-clamped 2T NEM switches *in situ*. Fig. 4.8 (a) compares the switch-ON voltage using DC field only with that obtained by using the combined AC-DC field. In the former, a sharp current increase was observed at 13.8 V. By adding an AC component with a frequency 610.8 kHz which had a value close to the fundamental resonant frequency of the nanowire f_0 = 623 kHz with amplitude $V_{ON,\ AC}$ = 0.45 V, switch-ON event was registered at $V_{ON,\ DC}$ = 5.0 V, thus decreasing V_{ON} by more than two times. Fig. 4.8 (b) shows how ON-state current depends on time while cycling a Bi_2Se_3 nanobelt-based NEM switch. For Bi_2Se_3, the combined AC-DC actuation was the only mode that allowed repeatable operation of this switch, because it allowed to decrease the current during the switching-ON. In the case of DC-only actuation, the structural degradation of the nanobelt was observed, most likely due to the high current pulses experienced during the contact formation.

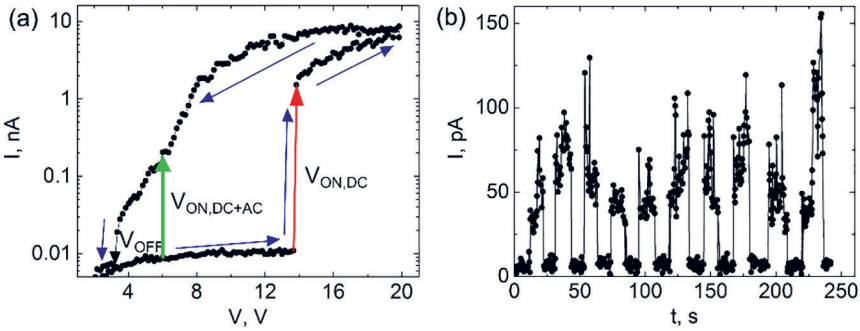

Figure 4.8. **Reduction of switch-ON voltage in a NEM switch with AC field. (a) NEM switch operation cycle. Using DC component only, the switch-ON is registered at 13.8 V (red line), while using AC–DC field, V_{ON} decreases down to 5.0 V (green line). (b) Current versus time graph, showing repeatable Bi_2Se_3 nanobelt switching, using AC-DC field**

4.4. Fabrication and characterization of integrated NEM switches

4.4.1. Calculation of the geometrical parameters for integrated NEM switches

The most important geometrical parameters of the simple-configuration NEM switches investigated in this thesis are radius/thickness and suspended length of the active element and its distance to the gate (G) electrode. To

calculate the geometry needed for fabrication of integrated CuO and Bi_2Se_3 NEM switches, the previously determined electromechanical properties and *in situ* measurement results were used. An operating voltage range was chosen to prevent degradation of the active element, while simultaneously ensuring a high enough current flow in the ON state for a good signal-to-noise ratio. This range was up to 50 V for CuO and up to 20 V for Bi_2Se_3 1D NS. Geometrical parameters corresponding to the operating voltage range were calculated using an analytical–numerical model that will be explained below.

To calculate the switching-ON voltage V_{ON}, Euler-Bernoulli equation for a double-clamped cylindrical nanowire with length L_0 upon which there acts an electrostatic force was expressed as:

$$Y^{(4)}(\xi) - F_x(\xi)Y^{(2)}(\xi) - F_E(\xi) = 0, \xi = \frac{L}{L_0} \tag{4.4}$$

In equation (4.4) Y stands for the displacement in the direction perpendicular to the nanowire, ξ – normalized coordinate along the nanowire, F_x – tension force, F_E – linear density of electrostatic force. Upper indices in parentheses denote derivatives over the normalized coordinate.

The electrostatic force was expressed as

$$F_E = \frac{16}{EL_0R^4}\frac{V^2\varepsilon_0}{\sqrt{z^2 - R^2}\,Lnc^2}, c = \frac{2z^2}{R^2}\left(1 - \sqrt{1 - \frac{R^2}{z^2}}\right) - 1, \tag{4.5}$$

where

$$z = z_0 + Y(\xi) \tag{4.6}$$

In eq. (4.6.), z_0 is the initial and z – the variable distance from the nanowire axis to the G electrode.

Tension force F_x was calculated as

$$F_x = \frac{4}{R^2}\left[1 - \int_0^1 \sqrt{(1 - \left(Y^{(1)}(\xi)\right)^2}\,d\varepsilon\right] \tag{4.7}$$

Using boundary conditions for a double-clamped nanowire, equations (4.4)–(4.7) were solved numerically for a set of increasing values of electric voltage. The threshold voltage, above which the solution could no longer be found (i.e., the deformed nanowire intersected the surface of the counter electrode) was reported as V_{ON}.

NEM switch V_{ON} values as a function of size and distance to the G electrode are depicted graphically in fig. 4.9 for a CuO nanowire-based switch at room temperature. The values were calculated assuming 155 GPa as the mean value of Young's modulus in this diameter range.

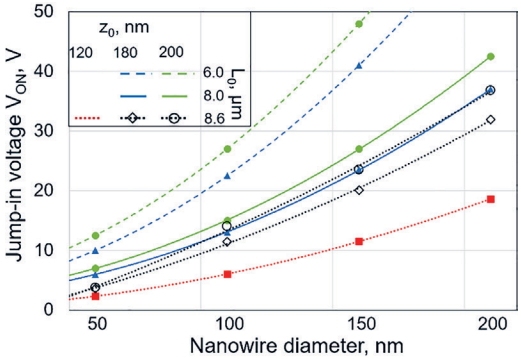

Figure 4.9. **Calculation of CuO nanowire-based NEM switch V_{ON} as a function of nanowire diameter d. z_0 – distance to the G electrode, L_0 – suspended length of the nanowire. Curves are added through the data points as guides to the eye. The dashed curve corresponds to L_0 = 6.0 µm, the solid curve to L_0 = 8.0 µm and the dotted curve to L_0 = 8.6 µm. The red square corresponds to z_0 = 120 nm, the blue triangle to z_0 = 180 nm and the green circle to z_0 = 200 nm**

4.4.2. Summary of the fabricated integrated NEM switches

The geometry of the integrated NEM switches was determined by considering the morphology, electrical and mechanical properties and operating voltage range investigated throughout the previous sections. The fabricated on-chip NEM switches were characterized in an optical microscope, SEM and AFM multiple times during the fabrication and operation testing. Fig. 4.10 shows a Bi_2Se_3-based NEM switch with a length of 3.3 µm determined by SEM, distance to the G electrode 190 nm and thickness 51 nm, both determined by AFM. Part of the suspended active elements exhibited a uniform deformation profile across the G electrode (fig. 4.10.(a)), while the other part – ununiform (fig. 4.10. (b)), which was taken into account when calculating the expected V_{ON} values.

Table 4.1 summarizes the geometrical parameters, elastic parameters and calculated and experimentally obtained V_{ON} values for in total of 10 CuO and Bi_2Se_3 NEM switches. Diameters of CuO NEM switch active elements were in the range from 50 nm to 210 nm, and thicknesses of Bi_2Se_3 NEM switch active elements were in the range from 51 nm to 145 nm. The distances from the active element to the G electrode varied from 120 nm to 200 nm and experimentally obtained V_{ON} values from 4.5 V to 49 V. All the switches in Table 4.1. have bottom contacts that are based on the adhesive interaction between the active element and underlying thin film electrode (S and D), with no extra contact from the top of the nanostructure.

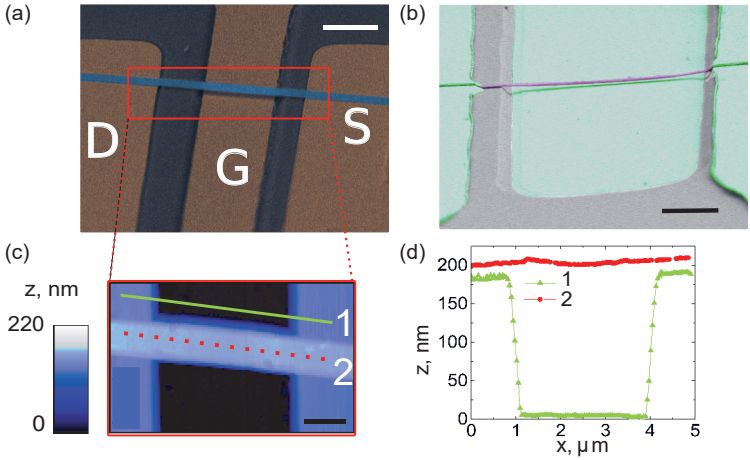

Figure 4.10. **Characterization of the fabricated integrated NEM switches. (a) False-coloured SEM image showing NEM switch with designated S, D and G electrodes. (b) NEM switch with uneven distance between the active element and the electrode. (c) AFM height image of the highlighted area in (a) for determination of the distance between the nanobelt and the G electrode, the deformation profile and thickness of the nanobelt. (d) Line profiles for AFM image in (c)**

Table 4.1. **Summary of fabricated and characterized integrated CuO and Bi_2Se_3 NEM switch parameters. Geometrical parameters (diameter d/thickness t, suspended length L_0, distance to the G electrode z_0, area moment of inertia I) are noted together with the corresponding elastic force F_{elas} and experimental $V_{ON,exp}$ and calculated $V_{ON,calc}$ values**

NEM switch no.	d (t), nm	L_0, μm	z_0, nm	I × 10^{-29}, m^{-4}	F_{elas}, nN	$V_{ON, exp}$, V	$V_{ON, calc}$, V
CuO-1	50	6.2	120	0.03	11.1	4.5	4.3
CuO-2	125	8.6	120	1.20	16.8	12	8.5
CuO-3	210	6.4	120	9.60	325	49	39
CuO-4	100	7.4	190	0.49	17.1	26	17
CuO-5	118	9.2	190	0.95	17.3	16	12
CuO-6	150	6.7	190	2.50	117	28	37
Bi_2Se_3-1	51	3.3	190	0.57	64.0	20	23
Bi_2Se_3-2	122	3.3	190	3.30	368	25	27
Bi_2Se_3-3	86	3.6	200	1.00	91.0	17	15
Bi_2Se_3-4	145	6.7	200	2.70	28.0	27	27

4.4.3. Integrated CuO NEM switches at room temperature

Fig. 4.11 (a) shows current-voltage dependence for the first 5 cycles at room temperature for a CuO nanowire-based NEM switch with diameter d = 150 nm, suspended length L_0 = 6.7 μm and gap height z_0 = 190 nm (CuO-6 in Table 4.1). It was observed that V_{ON} diminished with each cycle, while the ON and OFF state current values remained at constant values. The systematic changes of V_{ON} were attributed to mechanical relaxation on the CuO-bottom-contact interface, leading to the sliding of the nanowire. Similar effect of V_{ON} reduction during the initial stages of cycling for NEM switches without top contacts has been reported in the literature [15, 51].

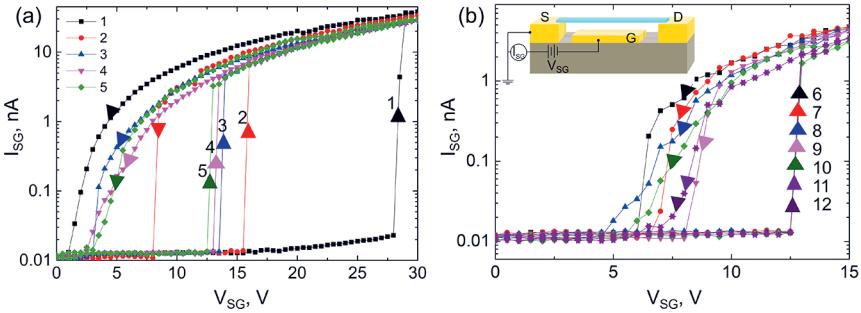

Figure 4.11. **Switching characteristics of an integrated CuO NEM switch during the initial cycles. (a) V_{ON} changes gradually from 28.0 V (black curve) to 12.5 V (green curve) during the first five cycles of operation. (b) Following the first cycles, a regime with constant V_{ON} of 12.5 V is established**

Starting from the fifth cycle, this switch exhibited a regime with a stable V_{ON} value of 12.5 V, while V_{OFF} stayed in the range from 2.5–3.5 V (fig. 4.11 (b)). In this constant voltage regime, extended NEM switch cycling was carried out to investigate the ON-state current evolution. Fig. 4.12 shows an excerpt of 5 switching cycles in time.

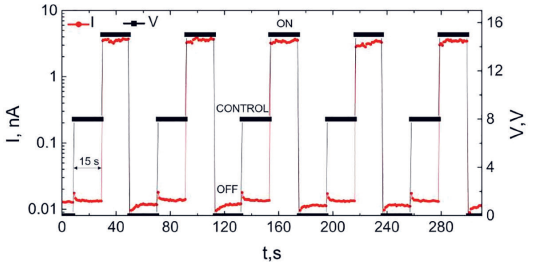

Figure 4.12. **A snippet from extended CuO NEM switch cycling, using actuation with a square voltage pulse. Red data points denote the current level in the OFF state (~0.01 nA, 0 V), control state (~0.01 nA, 8 V) and ON state (~4.0 nA, 15 V), controlled by the applied gate voltage (black data points)**

Three different direct voltage levels were applied in form of a square pulse: 0 V (OFF state), 8.0 V (control voltage), and 15 V (ON state). An intermediate state of control voltage was necessary to check if the nanowire had not made permanent contact with the G electrode. During 100 operating cycles, no significant increase was registered for the OFF state current, and no decrease for the ON state current.

4.4.4. Integrated Bi_2Se_3 NEM switches for operation at cryogenic temperatures

Conventional NEM switches

NEM switch operation was demonstrated at cryogenic temperatures, using Bi_2Se_3 nanobelts with bottom adhesive contacts as the active elements. The fabricated NEM switches had the following geometrical parameters of active element thicknesses of 51–145 nm, distances to the G electrode up to 200 nm and V_{ON} values of 8–27 V. For a typical Bi_2Se_3 NEM switch with L_0 = 3.3 μm, t = 51 nm, z_0 = 190 nm and w = 512 nm (Bi_2Se_3-1 in Table 4.1) the experimentally determined V_{ON} value at 5 K temperature was 20 V. NEM switches were implemented in different operating regimes. Non-volatile regime was implemented, when the adhesion force was larger than the electrical force after removal of the voltage, thus the active element stayed in contact. Non-volatile operation was manifested in the following sequence of I-V characteristics. The first cycle was a conventional NEM switching cycle with the sharp current jump (fig. 4.13 (a) cycle #1), followed by non-linear Schottky-type I-V with no current jumps (fig. 4.13 (a) cycle #2). Cycle #2 was attributed to the current flowing through the nanobelt in contact with the G electrode. By increasing the temperature to 300 K and repeatedly cooling down to 5 K, NEM switch exhibited another switching event with a sharp current jump (fig. 4.13 (a) cycle #3). Similar memory element function, only without returning to OFF state, was realized previously with Si and Ge nanowires [10].

A volatile operating regime, where the nanobelt returns to its initial state after removal of the voltage was implemented in switches, where the elastic force exceeded the adhesion force in contact. Fig. 4.13 (b-c) shows the operation of a volatile switch with V_{ON} of 9.2 V at 10 K temperature. During the first three cycles, V_{ON} decreased gradually with every next cycle, reaching 8.0 V, similarly to the behaviour in the CuO NEM switch. In contrast with the CuO NEM switch, the Bi_2Se_3 NEM switch exhibited sharper transitions to the OFF state at approximately 2.3 V. The OFF state current level was approximately 0.1 nA and the ON state was 100 nA, resulting in ON/OFF value of 10^3. The average value of the subthreshold slope was 80 mV/current decade (fig. 4.13 (c)). This value exceeds the theoretical limit of MOSFET at room temperature, however, it could easily be decreased further by, for example, increasing current compliance in the circuit.

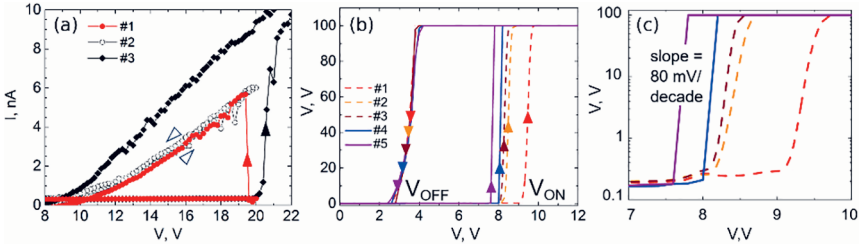

Figure 4.13. **Repeatable non-volatile (a) and volatile (b and c) Bi_2Se_3 NEM switch operation at 5 and 10 K temperatures. (a) The first switching cycle (red circles) is followed by a cycle with no sharp current jump (empty circles), followed again by a cycle with a sharp current jump (black diamonds) after a heating-cooling cycle. (b) Three cycles at 10 K (#1–#3, dashed curves), followed by two cycles at 5 K (#4–#5, solid curves). (c) I-V characteristics from (b) shown in log scale for the determination of the subthreshold slope value**

NEM switches with current control during the OFF-state

A conventional NEM switch does not present any means of extracting information about the deformation of the active element before contact establishment with the G electrode. To test the possibility of gaining information about the state of deformation from the current flowing through the nanostructure (between S and D electrodes), a 3T NEM switch was implemented. As the buckling deformation involves a sharp change from upwards to downwards bent state of deformation, when the force reaches the critical value, it could be expected that current changes would also be more pronounced. Therefore, a NEM switch with an upwards bent Bi_2Se_3 nanobelt was fabricated (fig. 4.14).

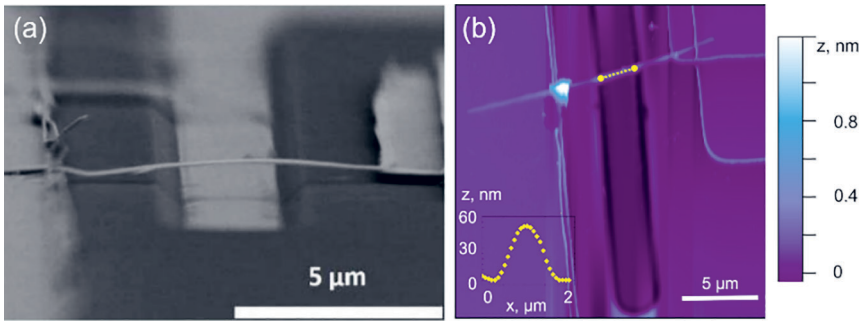

Figure 4.14. **(a) In-angle SEM image showing NEM switch with upwards curved Bi_2Se_3 nanobelt and its AFM image (b). The graph in the inset shows the height profile for the yellow line along the part of the nanobelt above the G electrode**

$V_{S\text{-}G}$ was applied between the nanobelt and the G electrode while monitoring resistance $R_{S\text{-}D}$ of the nanobelt. $V_{S\text{-}G}$ was gradually increased from 0 V to a maximum amplitude of 80 V with both positive and negative polarity at temperatures of 2 K and 4 K (fig. 4.15 (a)). Two linear regions with different slopes could be distinguished in the data, with slope change occurring at ±35 V gate voltage. This change was attributed to mechanical deformation of the nanobelt changing from upwards to downwards bent. Further voltage increase resulted in the gradual bending of the nanobelt towards the G electrode. To check this assumption of change of mechanical state during gating, the operation of the same NEM switch was characterized *in situ* SEM at room temperature (fig. 4.15 (e-f)). At similar $V_{S\text{-}G}$ values the transit of one state of mechanical deformation to another was confirmed both for negative and positive G voltages (fig. 4.15 (f)).

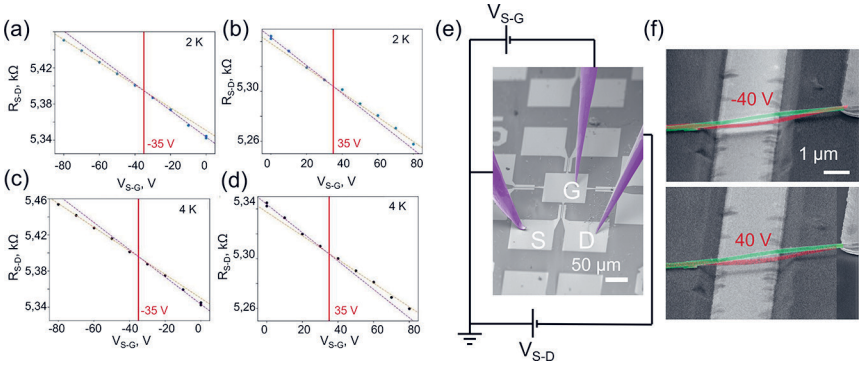

Figure 4.15. **$R_{S\text{-}D}$ as a function of $V_{S\text{-}G}$ at 2 K (a-b) and 4 K (c-d) temperature. The orange dashed line is a linear approximation for high electrical field values, violet – for low electrical field values. The vertical red line denotes $V_{S\text{-}G}$ value of ±35 V. (e) False-colored SEM image with the measured NEM switch *in situ* showing also the nanomanipulator electrodes (violet). (f) Overlayed false-coloured SEM images, confirming deformation of Bi_2Se_3 nanobelt, as the applied $V_{S\text{-}G}$ changed from 0 V (green) to critical voltage (red) value. The upper image corresponds to negative, lower – to positive $V_{S\text{-}G}$ polarity**

Implementation of S-D current monitoring in NEM switches would enable exact determination of the V_{ON} value. Also, at small nanobelt-gate distances it would be possible to access a regime with two currents in parallel, as S-G tunnelling current would contribute to the overall current. The geometry of the proposed NEM switch suggests that a top gate electrode can be implemented for additional control and could also be used as a non-volatile memory device due to its upwards bent shape.

CONCLUSIONS

1. For CuO nanowires, the required yield and geometric parameters with a mean diameter of approximately 70 nm and a mean length of 5 μm for application in NEM switches are achieved via electric field-enhanced oxidation on the cathode side in a wet air atmosphere. Synthesis on a 3 nm thick Au layer produces the optimal yield for NEM switch fabrication of approximately 100 Bi_2Se_3 nanobelts per 1000 μm^2 with mean lengths of 3 to 6 μm, and mean thicknesses within the range of 30 to 110 nm.
   These nanostructure dimensions enable reliable fabrication of NEM switches with repeatable operation. Further scaling would enable reduction of switch-ON voltage below 4 V.
2. The effective Young's modulus of CuO nanowires with diameters smaller than 50 nm is found to exhibit size dependence, increasing up to 550 GPa. For Bi_2Se_3 nanobelts Young's modulus is found to remain at a constant average value of 44 GPa in the examined thickness range from 35 nm to 171 nm.
   A method for electrical characterization of mechanical vibrations of double-clamped nanostructures as a function of temperature in the temperature range from 5 K to 300 K and frequencies up to 10 MHz is developed. Using this method, Bi_2Se_3 nanobelts exhibit strong temperature-dependent vibrations, that could possibly be explained by differential thermal expansion of the nanobelt-electrode-substrate system.
4. A process flow for bottom-up integrated NEM switch fabrication is developed using photo- and electron beam lithography. Using this process flow, single CuO nanowire and topological insulator Bi_2Se_3 nanobelt switches with gap heights from 120 nm to 200 nm are fabricated.
5. Repeatable operation of a two-terminal CuO nanowire-based NEM switches at room temperature is demonstrated. Switching for 100 cycles is demonstrated with stable switching-ON voltage of 12.5 V and stable ON-state current of approximately 4 nA. CuO nanowire NEM switches are thus suitable for robust high-voltage applications.
6. Volatile and non-volatile repeatable operation is demonstrated with Bi_2Se_3 nanobelt-based two-terminal NEM switches at temperatures as low as 5 K. It exhibits switching-ON voltage of 8.0 V, ON/OFF current ratio of 10^3 and a subthreshold slope of 80 mV/decade, which is close to the 60 mV/decade thermionic limit of electronic transistors at room temperature.
7. Bi_2Se_3 nanobelt-based three-terminal NEM switch with continuous current monitoring through the nanobelt during OFF state is demonstrated at 2 K temperature. This novel switching mode could enable precise determination of switch-ON voltage and increase switch reliability.

REFERENCES

[1] M. Muruganathan, N. H. Van, M. E. Schmidt, and H. Mizuta, *Advanced Functional Materials* **32**, 2209151 (2022).

[2] S. Saha, M. S. Baghini, M. Goel, and V. R. Rao, *IEEE Transactions on Electron Devices* **67**, 3894 (2020).

[3] T.-H. Lee, S. Bhunia, and M. Mehregany, *Science* **329**, 1316 (2010).

[4] Y. Qian, B. W. Soon, P. Singh, H. Campanella, and C. Lee, *Nanoscale* **6**, 5606 (2014).

[5] H. S. Kwon, J. W. Ko, and W. Y. Choi, *IEEE Electron Device Letters* **41**, 1257 (2020).

[6] Y. Li, E. Worsey, S. J. Bleiker, P. Edinger, M. Kumar Kulsreshath, Q. Tang, A. Yuji Takabayashi, N. Quack, P. Verheyen, W. Bogaerts, K. B. Gylfason, D. Pamunuwa, and F. Niklaus, *Nanoscale* **15**, 17335 (2023).

[7] X. Deng, N. Kang, and Z. Zhang, *Chip* **2**, 100064 (2023).

[8] J. Andzane, R. Meija, A. I. Livshits, J. Prikulis, S. Biswas, J. D. Holmes, and D. Erts, *Journal of Materials Chemistry C* **1**, 7134 (2013).

[9] J. Andzane, N. Petkov, A. I. Livshits, J. J. Boland, J. D. Holmes, and D. Erts, *Nano Letters* **9**, 1824 (2009).

[10] K. J. Ziegler, D. M. Lyons, J. D. Holmes, D. Erts, B. Polyakov, H. Olin, K. Svensson, and E. Olsson, *Applied Physics Letters* **84**, 4074 (2004).

[11] O. Y. Loh and H. D. Espinosa, *Nature Nanotechnology* **7**, 283 (2012).

[12] A. Peschot, C. Qian, and T.-J. K. Liu, *Micromachines* **6**, 1046 (2015).

[13] L. Wang, P. Zhang, Z. Liu, Z. Wang, and R. Yang, *Chip* 100038 (2023).

[14] M. Dequesnes, S. V. Rotkin, and N. R. Aluru, *Nanotechnology* **13**, 120 (2002).

[15] O. Loh, X. Wei, J. Sullivan, L. E. Ocola, R. Divan, and H. D. Espinosa, *Advanced Materials* **24**, 2463 (2012).

[16] X. L. Feng, M. H. Matheny, C. A. Zorman, M. Mehregany, and M. L. Roukes, *Nano Letters* **10**, 2891 (2010).

[17] G. M. Rebeiz, N. S. Barker, J. B. Muldavin, and G.-L. Tan, in *RF MEMS* (John Wiley & Sons, Ltd, 2003), pp. 21–57.

[18] C. Jia, Z. Lin, Y. Huang, and X. Duan, Chem. Rev. **119**, 9074 (2019).

[19] F. Marabelli, G. B. Parravicini, and F. Salghetti-Drioli, *Physical Review B* **52**, 1433 (1995).

[20] N. Kaur, M. Singh, and E. Comini, *Langmuir* **36**, 6326 (2020).

[21] A. M. B. Gonçalves, L. C. Campos, A. S. Ferlauto, and R. G. Lacerda, *Journal of Applied Physics* **106**, 034303 (2009).

[22] G. Filipič and U. Cvelbar, *Nanotechnology* **23**, 194001 (2012).

[23] X. Jiang, T. Herricks, and Y. Xia, *Nano Letters* **2**, 1333 (2002).

[24] C. Tang, X. Liao, W. Zhong, H. Yu, and Z. Liu, *RSC Advances* **7**, 6439 (2017).

[25] C. H. Xu, C. H. Woo, and S. Q. Shi, *Superlattices and Microstructures* **36**, 31 (2004).

[26] Y. Xia, D. Qian, D. Hsieh, L. Wray, A. Pal, H. Lin, A. Bansil, D. Grauer, Y. S. Hor, R. J. Cava, and M. Z. Hasan, *Nature Physics* **5**, 398 (2009).

[27] A. Ambrosi, Z. Sofer, J. Luxa, and M. Pumera, *ACS Nano* **10**, 11442 (2016).

[28] Y. Ando, *Journal of the Physical Society of Japan* **82**, 102001 (2013).

[29] S. N. Shirodkar, G. M. Stephen, A. T. Hanbicki, A. L. Friedman, and P. Dev, *Journal of Physical Chemistry C* **126**, 16877 (2022).

[30] G. Kunakova, L. Galletti, S. Charpentier, J. Andzane, D. Erts, F. Léonard, C. D. Spataru, T. Bauch, and F. Lombardi, *Nanoscale* **10**, 19595 (2018).

[31] S. M. Young, S. Chowdhury, E. J. Walter, E. J. Mele, C. L. Kane, and A. M. Rappe, *Physical Review B* **84**, 085106 (2011).

[32] D. Flötotto, Y. Bai, Y.-H. Chan, P. Chen, X. Wang, P. Rossi, C.-Z. Xu, C. Zhang, J. A. Hlevyack, J. D. Denlinger, H. Hong, M.-Y. Chou, E. J. Mittemeijer, J. N. Eckstein, and T.-C. Chiang, *Nano Letters* **18**, 5628 (2018).

[33] C. Schindler, C. Wiegand, J. Sichau, L. Tiemann, K. Nielsch, R. Zierold, and R. H. Blick, *Applied Physics Letters* **111**, 171601 (2017).

[34] L. T. Ngo, D. Almécija, J. E. Sader, B. Daly, N. Petkov, J. D. Holmes, D. Erts, and J. J. Boland, *Nano Letters* 6, 2964 (2006).

[35] R. Meija, J. Kosmaca, L. Jasulaneca, K. Petersons, S. Biswas, J. D. Holmes, and D. Erts, *Nanotechnology* **26**, (2015).

[36] M. Aghazadeh Meshgi, S. Biswas, D. McNulty, C. O'Dwyer, G. Alessio Verni, J. O'Connell, F. Davitt, I. Letofsky-Papst, P. Poelt, J. D. Holmes, and C. Marschner, Chemistry of Materials **29**, 4351 (2017).

[37] J. Andzane, G. Kunakova, S. Charpentier, V. Hrkac, L. Kienle, M. Baitimirova, T. Bauch, F. Lombardi, and D. Erts, *Nanoscale* **7**, 15935 (2015).

[38] E. P. S. Tan, Y. Zhu, T. Yu, L. Dai, C. H. Sow, V. B. C. Tan, and C. T. Lim, *Applied Physics Letters* **90**, 163112 (2007).

[39] G. Wang and X. Li, Journal of Applied Physics **104**, 113517 (2008).

[40] L. Fang, Y. Jia, D. J. Miller, M. L. Latimer, Z. L. Xiao, U. Welp, G. W. Crabtree, and W.-K. Kwok, *Nano Letters* **12**, 6164 (2012).

[41] S. Giraud, A. Kundu, and R. Egger, *Physical Review B* **85**, 035441 (2012).

[42] A. Cavallin, V. Sevriuk, K. N. Fischer, S. Manna, S. Ouazi, M. Ellguth, C. Tusche, H. L. Meyerheim, D. Sander, and J. Kirschner, *Surface Science* **646**, 72 (2016).

[43] Y. Xu, C. Chen, V. V. Deshpande, F. A. DiRenno, A. Gondarenko, D. B. Heinz, S. Liu, P. Kim, and J. Hone, *Applied Physics Letters* **97**, 243111 (2010).

[44] C. B. Maliakkal, J. P. Mathew, N. Hatui, A. A. Rahman, M. M. Deshmukh, and A. Bhattacharya, J*ournal of Applied Physics* **118**, 114301 (2015).

[45] R. G. DeAnna, S. Roy, C. A. Zorman, and M. Mehregany, *Proc. Int. Conf. Modeling and Simulation of Microsystems*, 644–647 (1999).

[46] L. He, F. Xiu, Y. Wang, A. V. Fedorov, G. Huang, X. Kou, M. Lang, W. P. Beyermann, J. Zou and K. L. Wang, *Journal of Applied Physics* **109**, 103702 (2011).

[47] W. J. Wang, K. H. Gao, and Z. Q. Li, *Scientific Reports* **6**, 25291 (2016).

[48] J. Wang, A. M. DaSilva, C.-Z. Chang, K. He, J. K. Jain, N. Samarth, X.-C. Ma, Q.-K. Xue, and M. H. W. Chan, *Physical Review B* **83**, 245438 (2011).

[49] S. Hikami, A. I. Larkin, and Y. Nagaoka, *Progress of Theoretical Physics* **63**, 707 (1980).

[50] S. Matsuo, K. Chida, D. Chiba, T. Ono, K. Slevin, K. Kobayashi, T. Ohtsuki, C.-Z. Chang, K. He, X.-C. Ma, and Q.-K. Xue, *Physical Review B* **88**, 155438 (2013).

[51] P. Ryan, Y.-C. Wu, S. Somu, G. Adams, and N. McGruer, J*ournal of Micromechanics and Microengineering* **21**, (2011).

ACKNOWLEDGEMENTS

I would like to thank my supervisor, Donats Erts, a pioneer of significant developments in the field, for introducing me to and guiding me through the exciting world of nanoelectromechanics. I enjoyed your relentlessness, creative and sometimes nearly-impossible-to-implement ideas, as well as your ability to question the results and focus on the big and small picture of the scientific research.

My colleagues at the Institute of Chemical Physics sustained my motivation throughout many years by being passionate, funny, patient and by simply being who they are. Special thanks to the nanoelectromechanics group: Lena, Raimonds, Raitis, Juris, Alexander Livshits, Jana, Edijs, Matiss. Thanks to Elza, for being with me through the loneliest phase of the research. I learnt quite a lot from all of you, and it was a pleasure working together.

Thanks to my colleagues at the Institue of Solid State Physics for their cooperation, support, and for introducing me to the exciting world of micro- and nanofabrication.

And finally, thanks to Elina, Vyacheslavs, Kiryl and Gunta for trying to explain things that are hard to understand.

Most importantly, thanks to my family and friends, especially my daughter Emma, for saying that if grown-ups have such boring occupations as mine, she would rather not grow up. (I am looking forward to your thesis).